Characterization of Photodiodes for Detection of Variations in Part-to-Part Gap and Weld Penetration Depth During Remote Laser Welding of Copper-to-Steel Battery Tab Connectors

Giovanni Chianese
Department of Industrial Engineering,
University of Naples Federico II,
P.le V. Tecchio,
Naples 80125, Italy
e-mails: giovanni.chianese@unina.it;
Giovanni.Chianese@warwick.ac.uk

Pasquale Franciosa
WMG,
University of Warwick,
Coventry CV4 7AL, UK
e-mail: p.franciosa@warwick.ac.uk

Jonas Nolte
Precitec GmbH & Co. KG,
Gaggenau 76571, Germany
e-mail: j.nolte@precitec.de

Darek Ceglarek
WMG,
University of Warwick,
Coventry CV4 7AL, UK
e-mail: d.j.ceglarek@warwick.ac.uk

Stanislao Patalano
Department of Industrial Engineering,
University of Naples Federico II,
P.le V. Tecchio,
Naples 80125, Italy
e-mail: patalano@unina.it

This paper addresses sensor characterization to detect variations in part-to-part gap and weld penetration depth using photodiode-based signals during remote laser welding (RLW) of battery tab connectors. Photodiode-based monitoring has been implemented largely for structural welds due to its relatively low cost and ease of automation. However, research in sensor characterization, monitoring, and diagnosis of weld defects during joining of battery tab connectors is at an infancy and results are inconclusive. Motivated by the high variability during the welding process of dissimilar metallic thin foils, this paper aims to characterize the signals generated by a photodiode-based sensor to determine whether variations in weld quality can be isolated and diagnosed. Photodiode-based signals were collected during RLW of copper-to-steel thin-foil lap joint (Ni-plated copper 300 μm to Ni-plated steel 300 μm). The presented methodology is based on the evaluation of the energy intensity and scatter level of the signals. The energy intensity gives information about the amount of radiation emitted during the welding process, and the scatter level is associated with the accumulated and un-controlled variations. Findings indicated that part-to-part gap variations can be diagnosed by observing the step-change in the plasma signal, with no significant contribution given by the back-reflection. Results further suggested that over-penetration corresponds to significant increment of the scatter level in the sensor signals. Opportunities for automatic isolation and diagnosis of defective welds based on supervised machine learning are discussed. [DOI: 10.1115/1.4052725]

Keywords: advanced materials and processing, inspection and quality control, laser processes, sensors, welding and joining

Introduction

The transition from fossil fuel to electric mobility has influenced the industrial strategies of many automakers to produce a significantly higher share of electric vehicles [1]. Large-scale battery manufacturing is, therefore, rapidly emerging as an industry priority.

Battery packs are commonly designed and manufactured in a pack-module-cell structure. Hence, based on the desired pack capacity and power, a suitable number of cells are clustered into a module and all the modules are connected within the pack [2]. For example, a Tesla Model S has a battery pack with a power of 85 kW h, and the assembly process consists of more than 10,000 welds at cell and module levels and more than 30 m of weld seam length is necessary during the construction of a single battery pack [3,4]. It has been estimated that each Gigafactory produces approximately 6% defective cells and battery modules due to faulty welds [5]. Repair and re-work of defective welds, though possible, increase the tendency of defect formation (i.e., formation of cracks and intermetallics) and nonetheless would require auxiliary equipment, thereby increasing cost. Furthermore, since the individual components are too expensive to scrap (the cost of cells in a new battery represents around 64% of the total) and some (anode active material, cell separators, and electrolytes) are not fully recyclable (only 70–80% of the cell is currently

recyclable), manufactures have set stringent quality targets with weld reliability above 99.7%. This urgently calls for innovative solutions for better control of the weld quality. This paper aims to evaluate whether a photodiode-based sensor is able to detect variations of the weld penetration and part-to-part gap to enable in-process monitoring of remote laser welding (RLW) of battery tab connectors.

Welding of tab connectors must ensure that mechanical integrity, electrical conductivity, and thermal requirements are met with high repeatability. Connections resulting in unequal electrical resistances within the same battery pack result in uneven current loads that can reduce the overall electrochemical performance of battery pack and lead to inhomogeneous cell degradation [6].

With regard to welding technology, there is a growing interest in applying RLW in battery manufacturing due to several advantages such as single sided non-contact access, reduced and controlled heat input, and reduced processing time, with the possibility of making a single weld in fraction of a second, thereby enabling high throughput necessary for high production volume [2,7]. Kogel-Hollacher [8] estimates that between 60% and 80% of the overall production of a finished battery pack can be addressed by laser processing. Brand et al. [6] investigated and quantitatively compared resistance spot welding, ultrasonic welding, and RLW with regard to connecting cells in large battery assemblies and showed that the joints realized with laser welding were those with the lowest electrical contact resistance and the highest joint strength. They also observed that RLW is applicable to any cell type (either cylindrical, prismatic,

or pouch) made of dissimilar metals (i.e., steel, aluminum, and copper).

An important challenge to overcome is the limited or insufficient capability for in-process quality monitoring and control [9]. The quality of RLW weldments is generally assessed by measuring multiple features classified as (1) surface features (surface spatter, blowout, melt pool width, upper and bottom concavity, and seam discontinuity) and (2) sub-surface features (weld penetration depth, weld connection, porosity, and crack) [10]. State-of-the-art approaches for in-process monitoring involve the fusion of multiple sensors to detect multiple weld features [11]. For example, in-process monitoring of the surface features is a well-established area and comprises of complementary metal-oxide semiconductor (CMOS) and charged coupled device (CCD) camera-based or laser-based sensors that allow direct measurement of surface features [9]. At present, direct measurement of the sub-surface features remains outside the reach of current sensor technologies. In this context, Sokolov et al. [12] used optical coherence tomography (OCT) for direct measurement of weld penetration depth. They tested 450 μm thick aluminum to 300 μm thick copper using adjustable ring mode laser beam. Results showed that the OCT sensor was capable of direct measurement of weld penetration depth with accuracy of 100 μm, when compared to off-line/off-process metallographic analysis. Authors further concluded that the accuracy of the OCT measurement was highly sensitive to the selection of the welding process parameters. As such, the sensor needed to be re-calibrated every time any process parameters were about to be changed. Furthermore, the absence of the keyhole mode would have made the OCT sensor entirely unsuitable for measuring the weld penetration depth.

The sensitivity to welding process parameters is overcome by those sensors which passively observe the process emissions. They gather indirect signals via photodiodes, acoustic detectors, and/or spectrometers. Signals are then correlated to the weld features via statistical and machine learning techniques. Among those passive sensors, photodiodes have a simple structure at low cost and are suitable for providing information about the radiation from the metal vapor and plasma plume (S_P signal), the thermal condition of the processed zone (S_T signal), and the reflected laser light (S_R signal) [13].

The typical photodiode setup is illustrated in Fig. 1. The three sensors detect the radiation in three distinguished bandwidths. For example, for those process laser beams that emit in the near-infra-red (NIR) radiation, the typical bandwidths are S_P sensor—300–700 nm; S_R sensor—1020–1090 nm; S_T sensor—1200–2000 nm. It is worth noting that the S_T sensor observes the temperature of both molten pool and plasma plume [13].

Sanders et al. [14] showed that a photodiode-based sensor, which was sensitive to infra-red (IR) radiation emissions, was effective in monitoring changes in penetration depth. Park et al. [15] used two ultra-violet (UV) radiation sensors and one IR sensor in order to detect plasma and spatter generated during the laser welding of
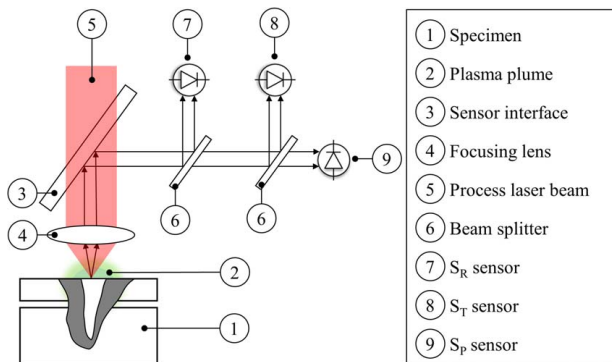
steel specimens with different thicknesses. Then, they developed a system to perform real-time evaluations of the weld quality using a data-driven model based on fuzzy multi-feature pattern recognition. However, no indication about the accuracy of the prediction model was reported. Rodil et al. [16] proposed two different approaches for in-process monitoring of galvanized steel (1 mm thick). The first approach was based on the decomposition of signals collected from IR and UV/visible photodiodes in both time and frequency domains. The accuracy of this approach was about 97% in defect detection with 6% misclassification rate for defect-free parts. The second approach consisted of relating the variations of the plasma electronic temperature with the weld quality. In order to gather radiation generated from the plasma plume, a naked optic fiber was placed facing the plume. Though the accuracy of this method was adequate, the equipment was much more complex and expensive than the photodiode-based sensor used in the first approach. Ozkat et al. [10] combined photodiode-based signal and physics-based simulation to model and estimate weld penetration depth and weld width during RLW of zinc-coated steel with thicknesses of 1 mm (top) and 1.2 mm (bottom). Their work also discussed a system for closed-loop quality control.

Photodiode-based monitoring has been mostly implemented for structural welds (i.e., door closures, seat frames, and side frames in automotive body construction) with thick parts generally above 1 mm [17]. However, the application of photodiode-based monitoring in the RLW of dissimilar metallic thin foils for battery cell manufacturing remains an unexplored area of research [9,18] and will be addressed in this paper.

At present, there are a number of challenges pertaining to RLW applications for joining dissimilar metallic thin foils for battery cell manufacturing. They include: challenge 1—control of cracking mechanisms and brittle intermetallic compounds. Welding of dissimilar metals with laser technology involves mixing of two materials with different thermal and mechanical properties which can lead to segregation and precipitates, poor compatibility and miscibility, and poor joint strength. Challenge 2—manufacturing and clamping tolerances, which can generate an accumulated part-to-part gap of more than 0.3 mm and, thereby, can lead to lack of joint connection. Challenge 3—temperature management during the joining process to avoid damage to battery cells and minimize the risk of fire and explosion due to over-heating or over-penetration welds.

In this paper, challenge 1 is solved by implementing the established technology of laser beam wobbling [19]; therefore, it is not discussed in detail. Challenges 2 and 3 are interdependent with each other and are motivated by the fact that variations in part-to-part gap and weld penetration depth, as shown conceptually in Fig. 2, have detrimental effects on both the structural and electrical integrity of the welds and the safety of the process. Indeed, variations in the geometry of the foils result in variations in part-to-part

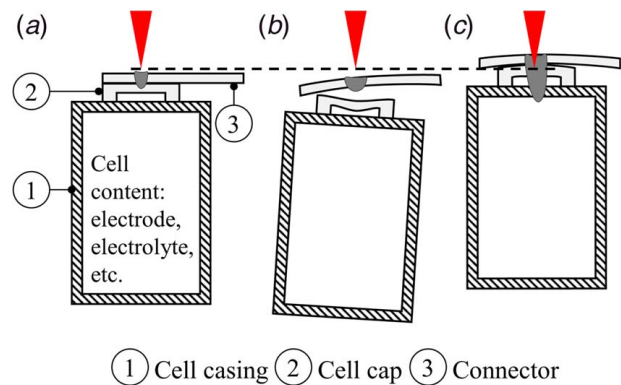Fig. 1 Standard concept of photodiode-based setup for in-process monitoring of the RLW process

Fig. 2 Typical design of a cylindrical cell and tab connector; (a) ideal welding condition, (b) actual welding condition, and (c) over-penetration

gap, which due to the small thicknesses of the parts being welded may lead to lack of connection or excessive seam concavity. The importance of detecting variations in the weld penetration depth is twofold: first, excessive weld penetration depth (Fig. 2(c)) brings the risk of piercing adjacent components (electrodes, etc.) with subsequent leakages of harmful gases and fire; second, lack of penetration (Fig. 2(b)) is associated to drop in electrical connection with subsequent reduction in electrical conductivity. The variation in weld penetration depth is the cumulative effect of variations in laser power, focal point shift, material reflection, etc. [20].

The paper will address challenges 2 and 3 and will use photodiode-based sensing techniques to determine if variations in weld quality can be isolated and diagnosed. The interest is in diagnosing defective weld conditions caused by part-to-part gap variations and/or excessive weld penetration depth. The paper will focus on RLW of copper-to-steel thin foils lap joint (Ni-plated copper 300 μm to Ni-plated steel 300 μm). Those materials are widely used for manufacturing of battery cells and tab connectors.

Materials and Methods

Experimental Configuration and Setup. The RLW experiments consisted of 300 μm-thick metal foils (oxygen free C103 copper R240, nickel-plated; steel plate cold deep, draw extra, nickel-plated), which were welded in lap configuration with welding length of 40 mm. The laser beam motion consisted of the superimposition of a linear motion, with a speed of 120 mm/s, and a circular wobbling with frequency of 500 Hz and a radius of 0.2 mm. The laser power (P_L) was delivered in continuous welding (CW) mode (no power modulation). The laser beam was perpendicular to the specimen (70 mm long and 30 mm wide). All the experiments were performed without shielding gas and without filler wire. Samples were wiped with acetone before welding to remove any surface contamination.

The employed laser unit was an nLight compact fiber laser 3 kW (nLight Inc., USA) and the laser beam was delivered by a 2D scanner (Scout-200, Laser & Control K-lab, South Korea).

The laser welding monitoring (LWM 4.0; Precitec GmbH, Germany) was used as photodiode-based sensor and was installed just below the collimator of the scanner, close to the camera port (see Fig. 3(a)). The sensor allows collecting the three signals, S_P, S_R, and S_T, at a maximum sampling rate of 50 kHz. The sensor was aligned to the center of the molten pool/keyhole. Full specifications of the welding setup are shown in Table 1.

The focal position was controlled by manually adjusting the Z position of the whole Scout-200 scanner on the mounting frame. The focal point was set at 600 μm above the bottom surface of the steel foil (see Fig. 3(b)).

Pictures of the front and back views were taken for each seam with a stereo microscope Nikon SMZ18. Metallographic analysis was conducted by cutting each seam into four cross sections, which were then grinded and polished (no etching)—details of
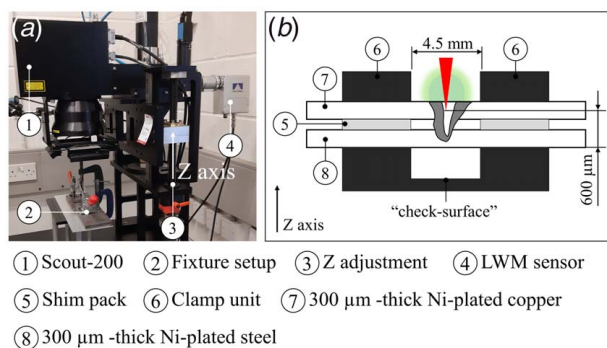
Table 1 Specification of the welding setup

Compact fiber laser, 3 kW, nLight	
Max. output power	3 kW
Wavelength range	1070 ± 10 nm
Beam quality	4 mm mrad
Fiber diameter	50 μm
Scout-200, Laser & Control K-lab	
Working field	70 mm × 70 mm
Collimating length	160 mm
Focal length	160 mm
Max. allowed laser power	2 kW
Spot diameter on focus	50 μm
Rayleigh length	0.8 mm

Table 2 Specification used for sample preparation with head speed of 60 rpm and force of 22 N

Operation	Grit size	Base speed (rpm)	Time (s)
Grinding	P400	220	Till plane
Grinding	P1200	220	60
Grinding	P2500	220	40
Grinding	P2500	220	40
Polishing	9 μm	150	350
Polishing	3 μm	150	180
Polishing	1 μm	150	120
Polishing	0.6 μm	150	90

the sample preparation are reported in Table 2. Pictures of the cross sections were taken with Nikon Eclipse LV150N.

Requirements and Design of Experiments. In order to validate the mechanical requirement, tensile shear tests were performed using Instron 5985 following ISO 6892-1:2016 tensile test standard. Tensile load was applied at a constant extension rate of 1 mm/min and the maximum loading was then extracted from the load-extension curve. The experiments were conducted in three phases: phase 1—definition of weld requirements and selection of welding parameters; phase 2—characterization of the photodiode-based signals to variations of weld penetration depth; and phase 3—characterization of the photodiode-based signals to variations of part-to-part gap. The execution order of the experiments in each phase was randomized to avoid bias effects.

Two geometric features (see Fig. 4) were measured for each cross section: (1) effective weld width (W_E) measured as the shortest distance from the root to the face of the weld and (2) bottom weld width (W_B) measured as the width of the weld at the back. The selection of W_B has been driven by the fact that the direct measurement of the weld penetration depth would have led to false positive/negative scenarios. Indeed, looking at Figs. 4(a) and 4(b), it appears that both cases (a) and (b) represent full-penetration welds (molten layer fully extended throughout the two foils). However, the case in Fig. 4(b) has a blind keyhole, which does not propagate throughout the bottom foil. As such, the laser radiation (shown as small linked arrows in Figs. 4(a) and 4(b)) eventually is only absorbed by the keyhole walls (or back-reflected towards the top) and does not

Fig. 3 (a) Experimental setup for collecting photodiode-based signals and (b) schematic view of the fixture setup

① Scout-200   ② Fixture setup   ③ Z adjustment   ④ LWM sensor

⑤ Shim pack   ⑥ Clamp unit   ⑦ 300 μm-thick Ni-plated copper
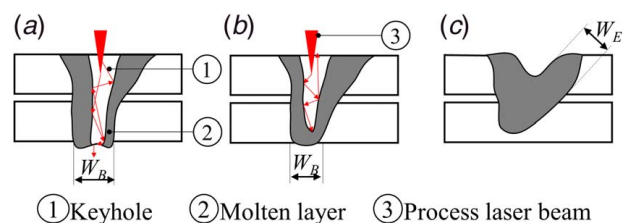
⑧ 300 μm -thick Ni-plated steel

Fig. 4 Definition of the weld features: (a) keyhole fully open throughout the bottom foil, (b) blind keyhole and (c) representation of weld seam in the general case
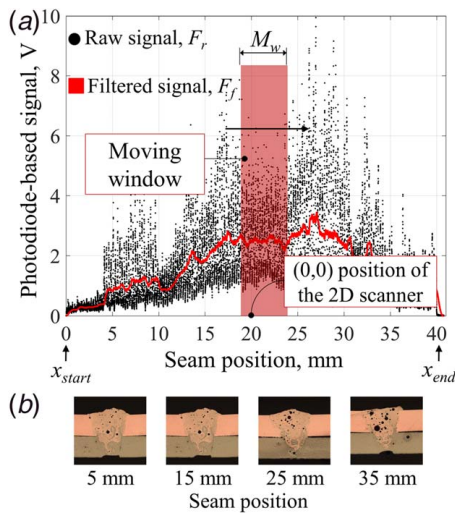
① Keyhole   ② Molten layer   ③ Process laser beam

Fig. 5 Example of photodiode-based signal: (a) raw signal and low-pass filtered signal and (b) cross sections of the corresponding seam

pierce through the bottom of the steel foil. Hence, case (b) compared to case (a) has limited/neglectable risk of laser beam piercing the adjacent components (electrodes, etc.).

Three classes of welds were introduced to account mechanical integrity, electrical resistance, and safety requirement:

- Class (1)—sound weld: $W_E \geq 220 \, \mu m$, $W_B \leq 0.6 W_E$
- Class (2)—lack of connection: $W_E \leq 220 \, \mu m$
- Class (3)—over-penetration: $W_B \geq 0.6 W_E$

Tensile shear test results conducted during phase (1) confirmed that W_E above 220 μm was sufficient to give 70 N/mm joint strength and minimum electrical resistance below 8 $\mu\Omega$ [19]. The over-penetration condition is controlled by W_B. We have assumed that the most severe welding condition from a safety standpoint corresponds to those cases with the keyhole fully open throughout the bottom foil (Fig. 4(a)). For each experiment, we have detected the mark left over by the laser beam on the "check-surface" as shown in Fig. 3(b). Pre-screening tests during phase (1) have confirmed that when W_B is greater than 60% of W_E, a visible mark is observed on the "check-surface." Those welds with $W_B \geq 0.6 W_E$ are then classified as over-penetration.

Weld penetration depth in phase (2) was varied by changing P_L in the range [600, 1500] W in order to achieve weld conditions spanning from lack of connection to over-penetration. Part-to-part gap was kept at zero. A total of 54 experiments were carried out in phase (2). For each power level, six replications were performed. Shim packs (Meusburger, Germany) of 12.5 mm width were employed in phase (3) to precisely control part-to-part gaps. The fixture setup (Fig. 3(b)) was designed to allow 4.5 mm clearance between the clamps to avoid heat sinking effects. A set of 16 experiments was carried out with the part-to-part gap varied in four levels: 0.0, 100, 200, 300 μm. For each gap level, four replications were performed.

Signal Processing. Figure 5 shows a typical photodiode-based signal, generated by the LWM sensor. The signal is represented
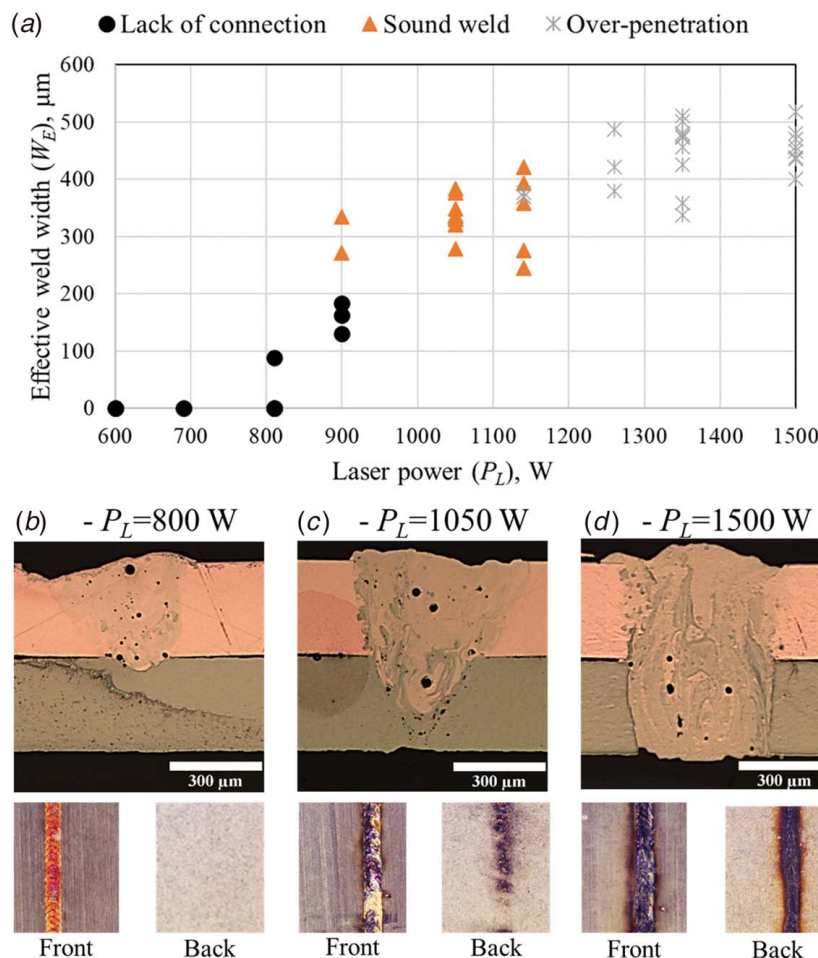

Fig. 6 (a) Results of the metallographic analysis for phase (2)—all welds at gap = 0 mm, (b) lack of connection, (c) sound weld, and (d) over-penetration
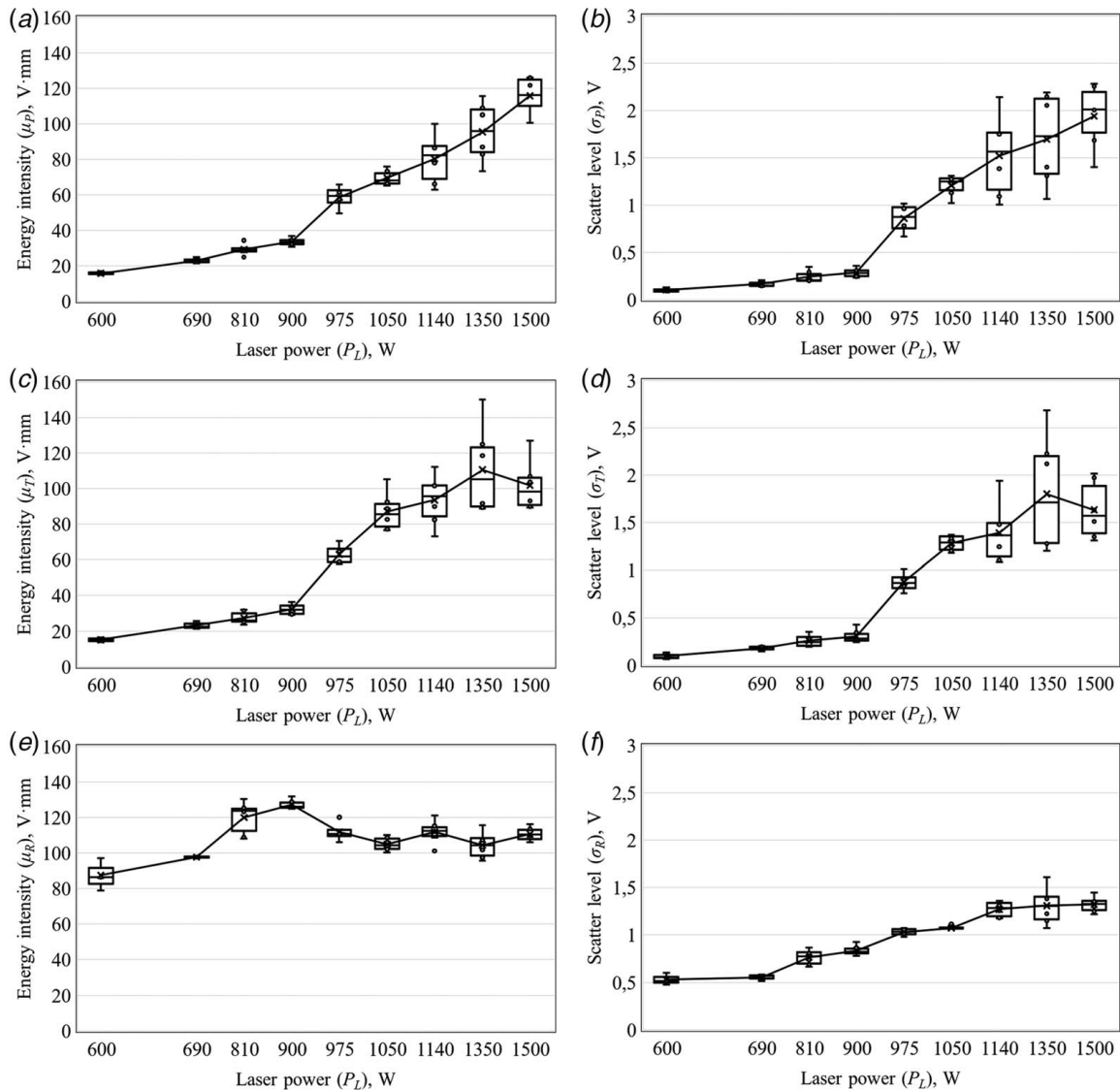
Fig. 7 Summary of the signal features extracted for phase (2)—characterization of the photodiode-based signals to variations of the laser power (all welds at gap = 0 mm)

in volt and both software and hardware gains have been calibrated and optimized to clamp the signals in the range [0, 10] V.

It is worth noting that the signal follows a behavior akin to a parabola (Fig. 5(a)). This is explained by the fact that the scanner Scout-200 spans the laser beam from the start to the end of the seam, which implies the rotation of the galvo-mirror. Since the

Fig. 8 Representative S_P signals of phase (2)—all weld at gap = 0 mm. (a) Lack of connection, (b) sound weld, and (c) over-penetration.

incidence angle changes along the seam, it is likely that the amount of process emission received by the LWM sensor changes with the incidence angle. This behavior only affects the signals but has negligible effect on the weld quality itself. This is confirmed by the cross sections in Fig. 5(b).

A low-pass filter has been implemented to remove high-frequency disturbances (above 100 Hz) from the raw signal, F_r, in order to obtain the filtered signal, F_f. Two features have been extracted from the signals:

- *Energy intensity*, μ, represents the total energy content of the emitted radiation. The energy intensity is defined (see Eq. (1)) as the area under the filtered signal (see Fig. 5(a)) from the seam start, x_{start}, to the seam end, x_{end}.
- *Scatter level*, σ, is the consequence of accumulated and un-controlled variations due to surface waviness, surface reflectivity, and molten pool dynamics. The source of noise related to signal-conditioning electronics is assumed invariant to the welding process itself, and therefore, neglected. The scatter level is defined as the averaged value of the local signal scatters, which are evaluated as the standard deviations, σ_i (see Eq. (2)), calculated on the raw data points that are within the moving window. The moving window scans the raw signal along the seam position, from start to end. The
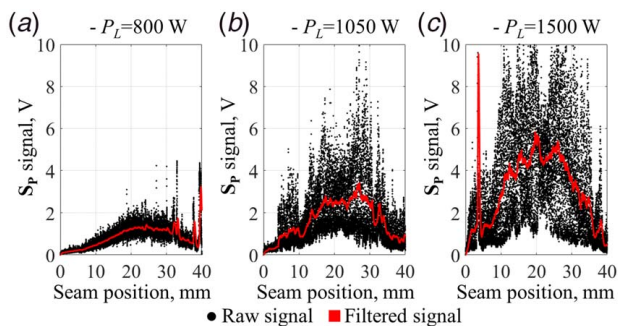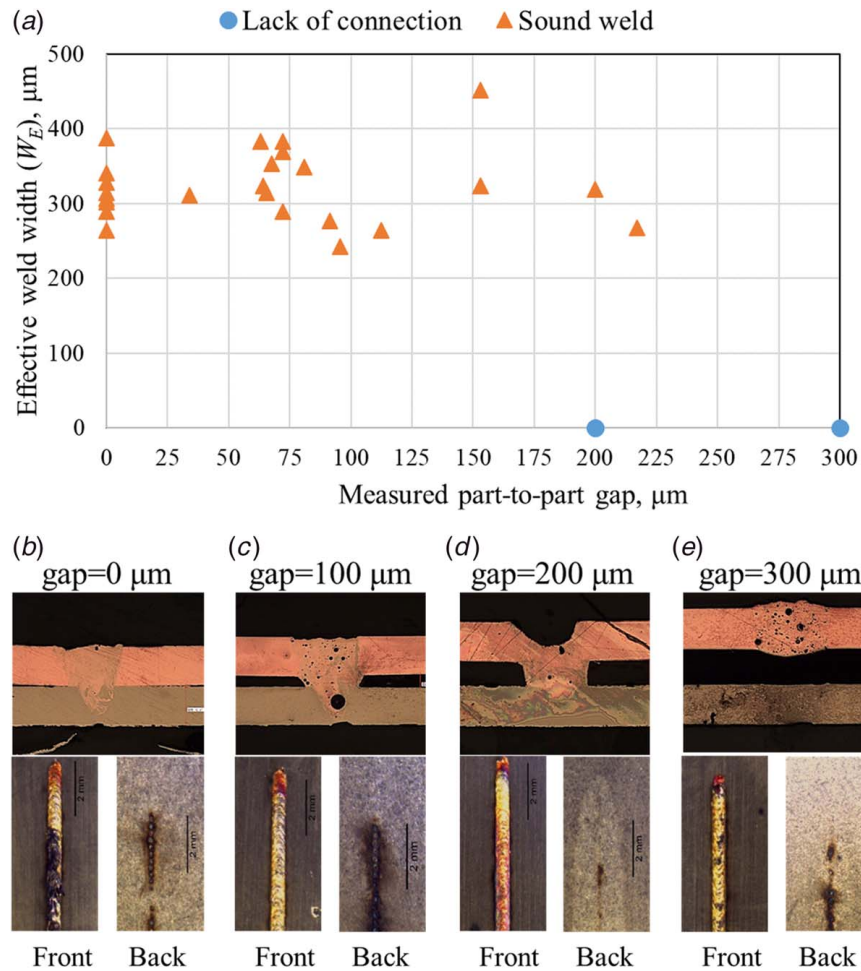
Fig. 9 (a) Results of metallographic analysis for phase (3)—all welds at $P_L = 1050$ W. (b, c) Sound weld and (d, e) lack of connection.

width (M_w) and the number of scans (N_s) of moving window were optimized via a sensitivity and convergence study during the preliminary welding trials of phase (1), which resulted in $M_w = 5$ mm and $N_s = 8$.

$$\mu = \int_{x_{start}}^{x_{end}} F_f(x)dx \tag{1}$$

$$\sigma = \frac{\sum_{i=1}^{N_s} \sigma_i}{N_s} \tag{2}$$

For each welding experiment, the sensor signals S_P, S_T, and S_R are then represented by the six-tuple $\{\mu_P, \mu_T, \mu_R, \sigma_P, \sigma_T, \sigma_R\}$.

The correlation between signals was quantified by Pearson's correlation coefficient. The value of the correlation ranges from -100% to 100%, where 0 indicates un-correlated signals.

Signals were grouped with respect to the three classes of welds as articulated in Sec. 2.2. Wilcoxon rank sum tests were performed in paired analysis to verify the null hypotheses that the values of signal features from different classes are sampled from distributions with equal medians at significance level of 5%. The non-parametric Wilcoxon rank sum test was selected to account data non-normality and heteroscedasticity between classes.

Results and Discussion

Phase (2)—Variations of Weld Penetration Depth. Weld penetration depth was varied by changing P_L in the range [600,

1500] W in order to achieve weld conditions spanning from lack of connection to over-penetration.

The results of the metallographic analysis are shown in Fig. 6. The graph reports the variation of the W_E against the variation in laser power, P_L. The data show a good linear correlation between W_E and P_L (Pearson's correlation coefficient: 89%). At up to 800 W, there is no connection at all (lack of connection) between the two foils. Between 900 and 1100 W, the welds exhibit satisfactory bonding area and no sign of over-penetration (sound weld). Above 1100 W, the molten pool fully extends throughout the two foils (over-penetration). It is worth noting that above 1100 W, the molten pool changes its shape from conical to cylindrical shape (as confirmed by the extent of the molten pool in Fig. 6(d)), indicating that the keyhole is now fully open throughout the bottom foil.

Figure 7 reports the summary of both energy intensity and scatter levels of the three signals—the spread across the six replications for each power level is shown via the box-plots. The height of the box-plot is a measure of the spread. Figure 8 shows three representative signals of the three classes—only the S_P signals have been reported for the sake of discussion. The result shows that there is a tendency towards higher energy and higher signal scatter with the increase of the laser power.

The findings are discussed as follows:

- Plasma and temperature signals (S_P and S_T)—positive strong correlation between the energy intensity of S_P and S_T and the laser power (Figs. 7(a) and 7(c))—Pearson's correlation coefficients are 95% and 87%, respectively. This suggests that the plasma plume emits not only in the UV/visible spectrum but
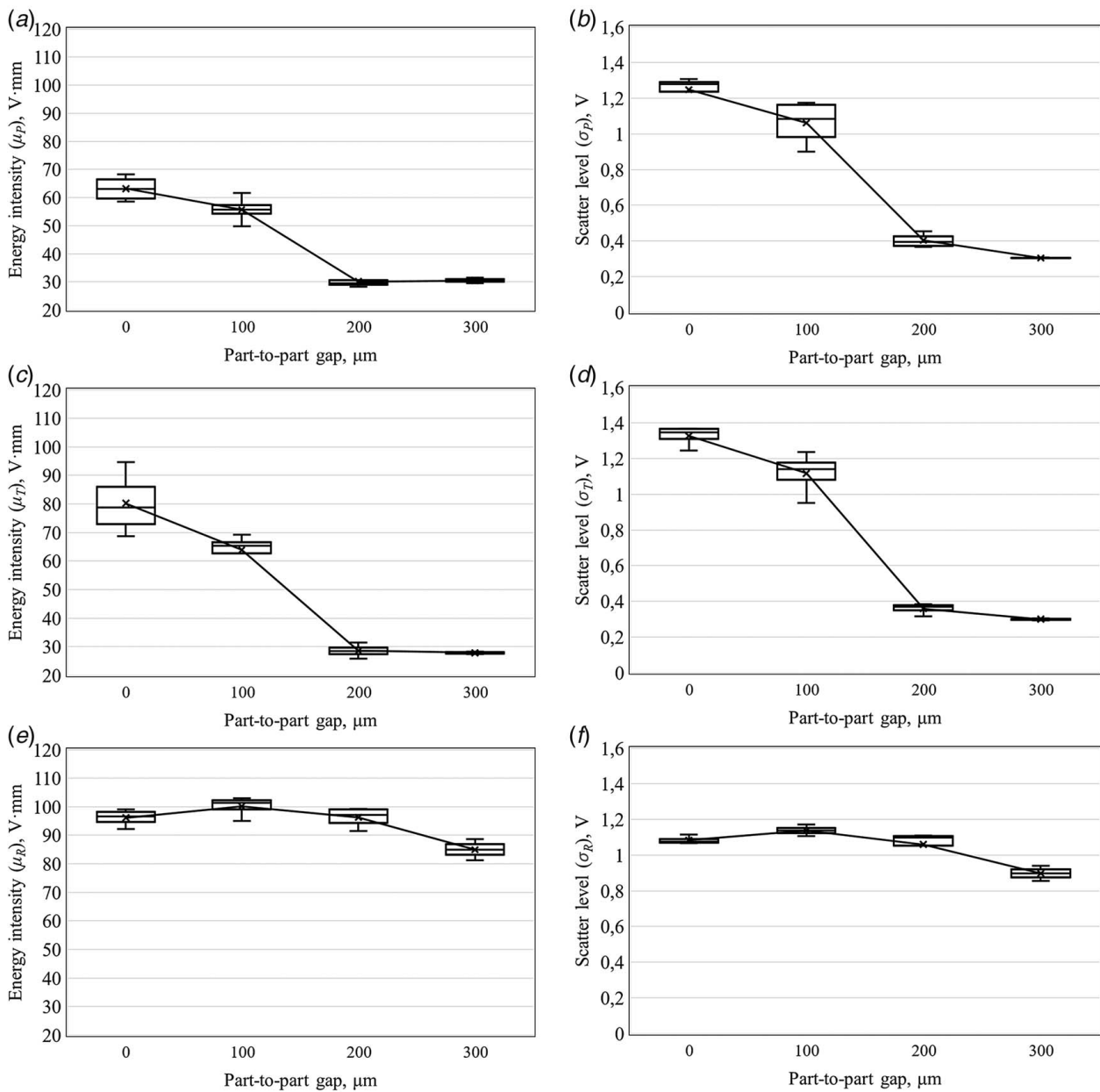
Fig. 10 Summary of the signal features extracted for phase (3)—characterization of the photodiode-based signals to variations of the part-to-part gap (all welds at $P_L = 1050$ W)

also contributes to the thermal radiation in the IR. The result agrees with the findings of Eriksson et al. [13]. Indeed, correlation analysis between features of signals S_P and S_T shows that these two signals are strongly correlated with Pearson's correlation coefficients above 94%.

The scatter level of S_P and S_T follows a similar trend (Figs. 7(b) and 7(d)), with Pearson's correlation coefficient of 89% and 85%, respectively. It is also of interest noting that when lower laser power is delivered to the processed zone (below 800 W), only the copper is molten with insufficient penetration depth through the steel foil; and since the welding regime is in conduction mode, the plasma level is significantly low (below 30 V mm).

- Back-reflection signal (S_R)—the energy intensity of the S_R signal is only weakly correlated to the laser power (Fig. 7(e)) with Pearson's correlation coefficient of 5%. Conversely, the scatter level (Fig. 7(f)) shows strong positive

correlation with Pearson's correlation coefficient of 90%. This result is interesting and shows that the local fluctuations are the symptom of sudden changes in the dynamics of the molten pool and the keyhole opening, with multi-reflections from the keyhole or from the molten pool itself.

- The spread in energy intensity and scatter level tends to increase significantly with the laser power. For example, for the energy intensity of the S_P signal (Fig. 7(a)), the spread goes approximately from 10 V mm to 40 V mm when transitioning from 1050 W (sound weld) to 1500 W (over-penetration). This evidence confirms that the transition to the over-penetration condition is characterized by higher instability of the keyhole and its oscillations, which is reflected by higher spread. Besides, the lower spread at power levels below 800 W confirms that the welding process tends to be more stable since it is in conduction mode. However, no or limited weld connection is achieved.

- Paired analysis via hypothesis tests confirmed that with the only exception of μ_R, differences between the values of the

signal features corresponding to the three classes of welds are statistically different at 5% significance level. Therefore, signal features $\{\mu_P, \mu_T, \sigma_P, \sigma_T, \sigma_R\}$ corresponding to different classes are statistically different and are good indicators for in-process monitoring and diagnosis of weld features.

Phase (3)—Variations of Part-to-Part Gap. Part-to-part gap varied in four levels: 0.0, 100, 200, 300 μm. The laser power was kept constant at 1050 W. The results of the metallographic analysis are shown in Fig. 9. The graph reports the variation of the W_E against the variation of the part-to-part gap. The data show a sudden drop in W_E after 200 μm part-to-part gap. This indicates the transition from sound weld to lack of connection.

Figure 10 summarizes the result of the signals processing with six synthetic plots that report the trend of the signal features with respect to the part-to-part gap. Figure 11 shows the plots of the S_P signals recorded during experiments with the four gap values considered. There is a tendency towards lower energy and lower signal scatter with the increase of the part-to-part gap. This is confirmed by the plots in Fig. 10.

The findings are discussed as follows:

- Back-reflection signal (S_R)—it has a weak contribution towards the detection and diagnosis of gap changes. Pearson's correlation coefficient is below 60% for both energy intensity and scatter level (Figs. 10(e) and 10(f)).
- Plasma and temperature signals (S_P and S_T)—descending trend is observed between the energy intensity of S_P and S_T, and the part-to-part gap (Figs. 10(a) and 10(c)) shows correlation coefficients of 89% and 88%, respectively. The scatter level follows a similar trend (Figs. 10(b) and 10(d)). The descending trend is explained considering that the greater the part-to-part gap, the higher the amount of plasma plume and the metal vapor entrapped between the two foils in the air channel between the foils. Therefore, the effective radiation emitted by the plume tends to drop with the increase in part-to-part gap. Strong correlation between these two signals is confirmed by correlation analysis with Pearson's coefficients above 98%.
- Temperature signal (S_T)—from a heat transfer standpoint, the surface temperature on the copper side would increase, when transitioning from sound weld (both in-plane and out-of-plane heat propagation) to lack of connection (only in-plane heat propagation). However, this is not reflected in the S_T signal, which, instead, tends to drop when the gap increases. This confirms the fact that the thermal radiation is the combination of both plasma plume and surface temperature emissions.
- The step-change in the behavior of the signal features $\{\mu_P, \mu_T, \sigma_P, \sigma_T\}$ are strong features to diagnose the transition from sound weld to lack of connection. The data show the presence of two clusters: gap = [0, 100] μm and gap = [200, 300] μm, with the transition to lack of connection in the range [100, 200] μm. The Wilcoxon rank sum tests confirmed that signal features $\{\mu_P, \mu_T, \sigma_P, \sigma_T\}$ corresponding to sound weld and lack of connection classes are statistically different (at 5% significance level) and are good indicators for detection of gap changes.

Future Opportunities

This research demonstrated that photodiode-based monitoring is a viable approach to detect variations of both part-to-part gap and weld penetration depth.

The methodology for signal processing was based on calculations involving two features: (1) energy intensity to represent the total energy content of the emitted radiation and (2) local signal scatter, which is the consequence of accumulated and un-controlled variations due to surface waviness, surface reflectivity, and molten pool dynamics. Results indicate that these two features are capable of detecting and diagnosing symptoms of the weld defects caused by variations of both part-to-part gap and weld penetration depth.
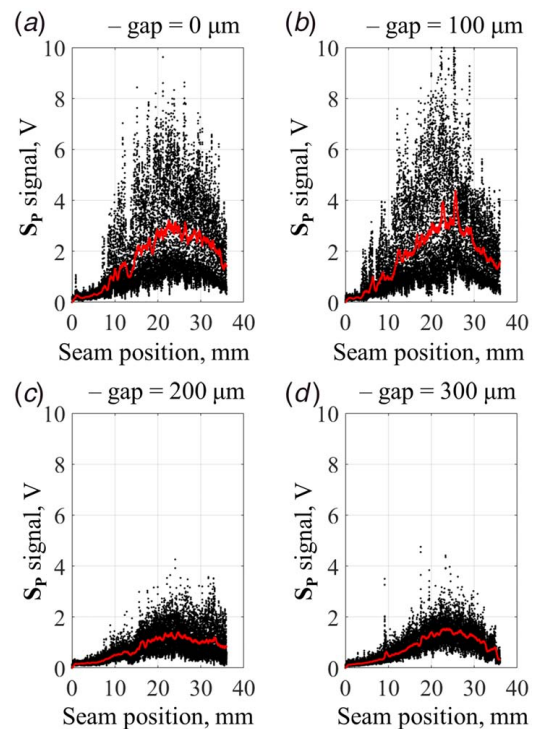

Fig. 11 Representative S_P signals of phase (3)—all welds at P_L = 1050 W. (a, b) Sound weld and (c, d) lack of connection.

This opens interesting opportunities for autonomous closed-loop control of weld quality with integrated photodiode-based sensors, powered-up by machine learning. For example, Fig. 12 illustrates the "feature space" which could be used to train a classification model and, therefore, drive towards a full autonomous and
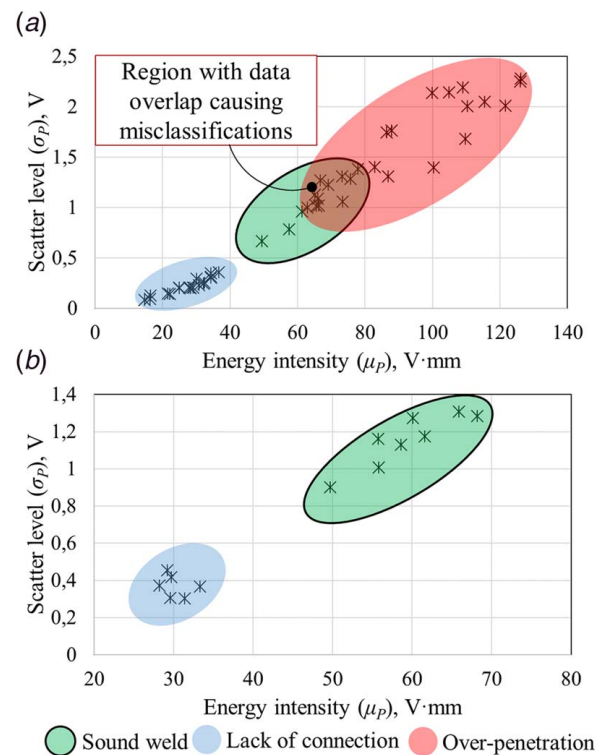

Fig. 12 Representation of the "feature space" for automatic diagnosis of weld defects. (a) Variations of laser power and (b) variations of part-to-part gap.

intelligent system for closed-loop quality control of laser weldments and root cause of weld defects [21].

Future work will investigate the combined effect of part-to-part gap and weld penetration depth. Attention will be posed at those regions of the "feature space" which overlap and clearly induce false negative (type-I error) and false positive (type-II error) scenarios. Furthermore, the correlation between the signal spread and the welding regime (either conduction or keyhole mode) will be further validated via high-speed camera.

Conclusions

The paper investigated photodiode-based signals to determine if variations in weld quality can be isolated and diagnosed during RLW of copper-to-steel thin-foil lap joint. The main interest was in diagnosing defective weld conditions caused by part-to-part gap variations and/or excessive weld penetration depth. Findings indicated that

- there exists a strong correlation (above 94%) between plasma and temperature signals. This suggests that the plasma plume emits not only in the UV/visible spectrum but also contributes to the thermal radiation in the IR;
- increasing weld penetration depth corresponds to significant increment of the energy intensity and the scatter level of signals S_P and S_T.
- energy intensity and scatter level of back-reflection have a weak contribution (absolute value of Pearson's correlation coefficient below 60%) towards the detection and diagnosis of variations in part-to-part gaps, and
- part-to-part gap variations can be diagnosed by observing the step-change in the plasma and temperature signals. Data highlighted that for part-to-part gap above 100 μm, the weldments exhibited a step-change from sound weld to lack or incomplete connection.

Conflict of Interest

There are no conflicts of interest.

Data Availability Statement

The datasets generated and supporting the findings of this article are obtained from the corresponding author upon reasonable request. The data and information that support the findings of this article are freely available.[1]

Nomenclature

M_w = width of the moving window (mm)
N_s = number of scans of the moving window

P_L = laser power (W)
S_P = signal generated by the radiation from plasma and metal vapor in the UV/visible (V)
S_R = signal generated by the reflected laser radiation in the NIR (V)
S_T = signal generated by the radiation in the short-wave IR radiation (V)
W_B = bottom weld width (μm)
W_E = effective weld width (μm)
μ_P, μ_T, μ_R = energy intensity of the signal S_P, S_T, and S_R (V mm)
$\sigma_P, \sigma_T, \sigma_R$ = scatter level of the signal S_P, S_T, and S_R (V)

References

[1] Burch, I., and Gilchrist, J., 2018, "Survey of Global Activity to Phase Out Internal Combustion Engine Vehicles," Center of Climate Protection, Santa Rosa, CA. https://theclimatecenter.org/wp-content/uploads/2020/04/Survey-on-Global-Activities-to-Phase-Out-ICE-Vehicles-04.06.2020.pdf
[2] Zwicker, M. F. R., Moghadam, M., Zhang, W., and Nielsen, C. V., 2020, "Automotive Battery Pack Manufacturing – A Review of Battery to Tab Joining," J. Adv. Join. Process., 1, p. 100017.
[3] Sun, T., Franciosa, P., Sokolov, M., and Ceglarek, D., 2020, "Challenges and Opportunities in Laser Welding of 6xxx High Strength Aluminium Extrusions in Automotive Battery Tray Construction," Procedia CIRP, 94, pp. 565–570.
[4] Sun, T., Franciosa, P., Liu, C., Pierro, F., and Ceglarek, D., 2021, "Effect of Micro Solidification Crack on Mechanical Performance of Remote Laser Welded AA6063 Fillet Lap Joint in Automotive Battery Tray Construction," Appl. Sci., 11(10), p. 4522.
[5] Sattar, A., Greenwood, D., Dowson, M., and Unadkat, P., 2020, "Automotive Lithium Ion Battery Recycling in the UK Based on a Feasibility Study."
[6] Brand, M. J., Schmidt, P. A., Zaeh, M. F., and Jossen, A., 2015, "Welding Techniques for Battery Cells and Resulting Electrical Contact Resistances," J. Energy Storage, 1, pp. 7–14.
[7] Ceglarek, D., Colledani, M., Váncza, J., Kim, D. Y., Marine, C., Kogel-Hollacher, M., Mistry, A., and Bolognese, L., 2015, "Rapid Deployment of Remote Laser Welding Processes in Automotive Assembly Systems," Ann. CIRP, 64(1), pp. 389–394.
[8] Kogel-Hollacher, M., 2020, "The Full Potential of Photonics in E-Mobility: An Overview," Laser User, 97, pp. 22–23.
[9] Cai, W., Wang, J., Jiang, P., Cao, L., Mi, G., and Zhou, Q., 2020, "Application of Sensing Techniques and Artificial Intelligence-Based Methods to Laser Welding Real-Time Monitoring: A Critical Review of Recent Literature," J. Manuf. Syst., 57, pp. 1–18.
[10] Ozkat, E. C., Franciosa, P., and Ceglarek, D., 2017, "A Framework for Physics-Driven In-Process Monitoring of Penetration and Interface Width in Laser Overlap Welding," 27 CIRP Design 2017, Cranfield, UK, May 10–12, pp. 44–49 [Procedia CIRP 60].
[11] Gao, X., Li, Z., Wang, L., Zhou, X., You, D., and Gao, P. P., 2019, "Detection of Weld Imperfection in High-Power Disk Laser Welding Based on Association Analysis of Multi-Sensing Features," Opt. Laser Technol., 115, pp. 306–315.
[12] Sokolov, M., Franciosa, P., Sun, T., Ceglarek, D., and Dimatteo, V., 2021, "Applying Optical Coherence Tomography for Weld Depth Monitoring in Remote Laser Welding of Automotive Battery Tab Connectors," J. Laser Appl., 33(1), p. 012028.
[13] Eriksson, I., Powell, J., and Kaplan, A. F. H., 2010, "Signal Overlap in the Monitoring of Laser Welding," Meas. Sci. Technol., 21(10), pp. 5705–5712.
[14] Sanders, P. G., Leong, K. H., Keske, J. S., and Kornecki, G., 1998, "Real-Time Monitoring of Laser Beam Welding Using Infrared Weld Emissions," J. Laser Appl., 10(5), pp. 205–211.
[15] Park, Y. W., Park, H., Rhee, S., and Kang, M., 2002, "Real Time Estimation of CO_2 Laser Weld Quality for Automotive Industry," Opt. Laser Technol., 34(2), pp. 135–142.
[16] Rodil, S. S., Arnanz Gómez, R., Bernárdez, J. M., Rodríguez, F., Miguel, L. J., and Perán, J. R., 2010, "Laser Welding Defects Detection in Automotive Industry Based on Radiation and Spectroscopical Measurements," Int. J. Adv. Manuf. Technol., 49(1–4), pp. 133–145.
[17] You, D., Gao, X., and Katayama, S., 2015, "WPD-PCA-Based Laser Welding Process Monitoring and Defects Diagnosis by Using FNN and SVM," IEEE Trans. Ind. Electron., 62(1), pp. 628–636.
[18] Stavridis, J., Papacharalampopoulos, A., and Stavropoulos, P., 2018, "Quality Assessment in Laser Welding: A Critical Review," Int. J. Adv. Des. Manuf. Technol., 94(5–8), pp. 1825–1847.
[19] Zapico, E. P., Ascari, A., Dimatteo, V., and Fortunato, A., 2021, "Laser Dissimilar Welding of Copper and Steel Thin Sheets for Battery Production," J. Laser Appl., 33(1), p. 012016.
[20] Seibold, M., Friedmann, H., Schricker, K., and Bergmann, J. P., 2020, "Process Control by Real-Time Pulse Shaping in Laser Beam Welding of Different Material Combinations," Procedia CIRP, 94, pp. 769–774.
[21] Franciosa, P., Sokolov, M., Sinha, S., Sun, T., and Ceglarek, D., 2020, "Deep Learning Enhanced Digital Twin for Closed-Loop In-Process Quality Improvement," CIRP Ann., 69(1), pp. 369–372.

[1]10.5281/zenodo.5115087